Effect of Zn addition on phase evolution in AlCrFeCoNiZn high-entropy alloy

Vikas Shivam[1,2 *], Dishant Beniwal[1], Yagnesh Shadangi[3,4], Prashant Singh[5], Olena Palasyuk[5], V.S. Hariharan[6], M.J. Kramer[5], G. Phanikumar[6], Duane D. Johnson[5,7], Pratik K. Ray[1*] and N.K Mukhopadhyay[3]

[1] Department of Metallurgical and Materials Engineering, Indian Institute of Technology Ropar, Rupnagar – 140001, Punjab, India.

[2] Department of Materials Science and Engineering, Seoul National University, Seoul, 08826, Republic of Korea

[3] Department of Metallurgical Engineering, Indian Institute of Technology (BHU), Varanasi – 221005, Uttar Pradesh, India.

[4]Department of Materials Science and Metallurgical Engineering, Indian Institute of Technology Bhilai, Durg 491001, Chhatishgarh, India

[5]Ames Laboratory, US Department of Energy, Ames, IA – 50011, USA

[6]Department of Metallurgical and Materials Engineering, Indian Institute of Technology Madras, Chennai – 600036, Tamil Nadu, India.

[7] Department of Materials Science & Engineering, Iowa State University, Ames, IA 50011, USA

***Corresponding Authors:**

Dr. Vikas Shivam (Email: vikas.rs.met13@iitbhu.ac.in)
Dr. Pratik K. Ray (Email: pratik@iitrpr.ac.in)
Department of Metallurgical and Materials Engineering,
Indian Institute of Technology Ropar, Rupnagar – 140001, Punjab, India.

Abstract

The addition of Zn to AlCrFeCoNi high-entropy alloy (HEA) poses intriguing questions as to how it would affect phase evolution. Here, the phase evolution in AlCrFeCoNiZn was studied using a combination of experimental techniques (XRD, SEM, EDS and DSC) and computational (density-functional theory (DFT), *cal*culation of *pha*se *d*iagrams (CALPHAD), and machine-learning) methods. Mechanically alloyed (MA) and spark plasma sintered (SPS) AlCrFeCoNiZn assumes a metastable single-phase, body-centered-cubic (BCC) structure that undergoes diffusion-controlled phase separation upon subsequent heat treatment to form separate (Al, Cr)-rich, (Fe, Co)-rich and (Zn, Ni)-rich phases. The formation of (Al, Cr)-rich phase, not reported previously in AlCrFeCoNi-based HEAs, is attributed to strong clustering tendency of (Cr-Zn) and (Cr-Ni) pairs, combined with the strong ordering of (Zn-Ni) pair, driving out Cr that in turn combines with Al to form a (Al, Cr)-rich phase. DFT results show the formation of thermodynamically stable $L1_2$ phase wherein Cr-Fe-Zn [Al-Ni-Co] preferably occupy *1a (000)* [*3c (0 ½ ½)*] positions. The sluggish diffusional transformation to $L1_2$ phase from BCC precursors is attributed to the small stacking-fault energy of AlCrFeCoNiZn. The equilibrated HEA exhibits a high microhardness of 8.24 GPa with an elastic modulus of 184 GPa.

Keywords: High-entropy alloy; Phase evolution; Mechanical alloying; Machine Learning; Density function theory

1. Introduction

High-entropy alloys (HEAs), from their inception [1,2], have garnered significant attention due to their superior thermodynamic, structural, and mechanical properties over conventional alloys [3–6]. Recently, Li et al. [7] have shown that mixing entropy alone is not sufficient to improve structure-property correlations in HEAs. The study introduces the idea of metastability created by compositional imbalance that significantly improved the mechanical properties of HEAs, opening exciting avenues for tailoring microstructure [7–10]. This suggests that competing effects of entropy, formation enthalpy, short-range ordering, and lattice strain (atomic-size mismatch) should be given due consideration for assessing thermodynamic stability and mechanical properties [9,11–13]. While the well-quantified rules governing phase evolution in HEAs are still an open question, the FCC↔BCC transitions in HEAs have been linked strongly to Valence-Electron Count (VEC) [14–16] wherein ($VEC < 6.87$), ($6.87 \leq VEC < 8$) and ($VEC \geq 8$) are generally associated with the formation of BCC, mixed FCC+BCC and FCC phases, respectively [15]. (CrFeCoNi)-based alloy systems have been amongst the most widely studied HEAs [17-20]. Addition of Al, with low VEC of 3, drives the transition from a single-phase FCC structure in CrFeCoNi (VEC=8) to a BCC structure in AlCrFeCoNi (VEC=7.2) [21,22]. In contrast, Zn, with its high VEC of 12, shows drastically different bonding tendencies with elements present in CrFeCoNi wherein it bonds strongly with Co and Ni and clusters strongly with Cr and Fe. Moreover, Zn is not a typical 3*d*-transition metal owing to its completely filled d-orbitals. This contrasting behavior of Zn and Al makes it interesting to observe phase evolution when both Al and Zn are added together to CrFeCoNi. With this as motivation, we present an in-depth study into the phase evolution in equiatomic AlCrFeCoNiZn.

The low boiling point of Zn, which is lower than the melting point of other elements here (except Al), makes the casting of AlCrFeCoNiZn challenging. Thus, MA+SPS route has been used for alloy fabrication. MA is a well-known technique to develop nanocrystalline alloys, oxide-dispersion strengthened (ODS) alloys, quasicrystals, amorphous alloys and composites with homogenous microstructure and extended solid solubility [23-25]. HEAs synthesized by MA have better mechanical properties due to grain refinement and solid-solution strengthening with homogenous mixing of alloying elements [26-30]. SPS is a solid-state sintering technique used for consolidation of alloyed powder prepared through MA. It is based on the concept of Joule heating wherein a high amperage current is passed to produce thermal energy that rapidly increases the material's temperature to form a dense product of nanometric grains.

The choice of processing route (as-cast or MA+SPS) can lead to different microstructures for the same HEA. As-cast AlCrFeCoNi HEA has a BCC structure with small amounts of (Al, Ni)-rich ordered B2 phase, and heat treatment at 850°C for 3h results in formation of new FCC and sigma (σ) phases along with the BCC and B2 phases [31,32].

The sigma phase is stable over a relatively small temperature range (roughly from 600 to 975°C) while the FCC remains stable up to 1200°C. AlCrFeCoNi prepared through MA+SPS (at 1000°C with a dwell time of 6 min) shows formation of an FCC solid-solution phase along with the precipitation of nano-sized (Fe, Co, Cr)-rich σ phase and (Al, Ni)-rich $L1_2$ phase [33]. Atom probe and TEM studies at nanometer scale have also confirmed phase separation in AlCrFeCoNi, driven by elemental segregation owing to strong Al-Ni and Fe-Cr ordering tendencies [34].

In view of this, the idea of Zn addition to AlCrFeCoNi poses some interesting and open questions with respect to the phase evolution in AlCrFeCoNiZn alloy:

a) Zn addition considerably increases the VEC from a value of 7.2 for AlCrFeCoNi to 8 for AlCrFeCoNiZn. From the VEC-based phase-selection criterion [15], wherein VEC ≥ 8 is generally associated with the formation of simple FCC solid-solution phases, will Zn addition destabilize BCC AlCrFeCoNi to form FCC or mixed phases?

b) Miedema's chemical enthalpies for binary pairs (i.e., sub-regular interaction parameters) indicate that both Zn and Al tend to bond strongly with Ni whereas Zn tends to cluster weakly with Al. One can therefore question the coexistence of (Al, Ni, Zn) in a single phase, and whether Zn added to AlCrFeCoNi HEA will form (Al, Ni, Zn)-rich phase or a segregated (Zn, Ni)-rich and (Al, Ni)-rich phases.

c) The Zn addition is expected to change the phase evolution in AlCrFeCoNi due to change in local thermodynamic short-range order, i.e., ordering or clustering type. How these thermodynamic changes might impact the formation of σ (Fe-Co-Cr rich) is not well understood. Furthermore, owing to large ordering tendency of Al-Ni pair, we usually do not expect the formation of new (Al, Cr)-rich ordering phases in AlCoCrFeNi-based HEAs. But Zn addition might affect this behavior; however, to the best of our knowledge, there are no such theoretical or experimental reports yet.

With these questions as the backdrop, we have performed an in-depth analysis of the phase evolution in AlCrFeCoNiZn. The multi-principal nature of HEAs necessitates the understanding of the phase evolution in different time-temperature scales. The type of phases and their fractions solely decided the properties of the materials. Moreover, the adoption of phase evolution in HEAs into engineering applications, especially alternatives to superalloys, will likely necessitate looking beyond single-phase solid-solution strengthening to achieve competitive results [35]. Pre-trained machine-learning (ML) models and CALPHAD calculations have been used to establish preliminary expectations of phase transitions, whereas X-ray Diffraction (XRD) and Energy Dispersive Spectroscopy (EDS) data have been analyzed for the identification of phase structures and elemental segregation. Density Functional Theory (DFT) calculations have been used to probe the drivers for phase

transitions and elemental segregation. Because SPS may not lead to formation of equilibrium structures, the effect of different heat treatments has also been studied. The insights gained from our work not only advance the understanding of this particular alloy, but also expand the general phase-selection principles for HEAs where strong ordering and clustering pairs are present.

2. Methodology

2.1. Experimental methods

High purity (>99%) elemental powders of Al, Co, Cr, Fe, Ni and Zn with average particle sizes of 45μm were used as the starting material. The initial mixture of the elemental powder was taken in equiatomic proportion, mixed at room temperature and subjected to the initial structural confirmation through X-ray diffraction (XRD). The mixed elemental powder was apportioned into two vials of 250 ml capacity, with 30 gm powder in each. Milling was carried out in a high-energy planetary ball mill (Retsch PM 400) using tungsten-carbide (WC) vials and balls of 10 mm diameter with the rotation speed of 200 rpm. The wet medium of milling was adopted by using toluene as a processing control agent (PCA) with a ball to powder ratio of 10:1. A definite protocol of milling was utilized, in which the mill was stopped for half an hour after every hour of milling to avoid the overheating of the vial temperature. The powder was collected at every 10h of milling to do the phase evolution study. Milling was done for a total of 30h duration to avoid the contamination of milled powder. The 30h milled powder was further subjected to consolidation through SPS at 800℃ with a holding time of 15 min under 50 MPa pressure. The SPS-prepared sample was further sectioned into three small pieces (diametrically) and sealed into the vacuum quartz tube for heat treatments. These quartz tubes were back-filled with argon gas to avoid the oxidation of samples. Two samples were heat-treated at 800℃ and 900℃ for 2h, followed by water quenching. In another case, a sample was heat-treated at 900℃ for the holding time of 12h, followed by furnace cooling to understand (by comparing with quenched samples) the extent to which kinetics affect the phase evolution.

XRD (Rigaku MiniFlex: 600 W; Cu Kα radiation, λ=1.541 Å) with a Bragg-Brentano geometry, operated at 20 kV and 40 mA with a scanning speed=10°/min, was used to study the structural changes in the milled, SPSed, and heat-treated samples. Additional x-ray diffraction studies were also carried out using a Co Kα radiation, λ=1.789 Å radiation in order to minimize fluorescence. The evolved phases were analyzed using the International Centre for Diffraction Data (ICDD) base software. The XRD data was processed through Rietveld refinement using the Generalized Structure Analysis System (GSAS-2) [36] to quantify the changes in the lattice parameter in milled and SPSed samples. The nanostructured nature of the 30h milled powder was confirmed through transmission electron microscopy (TEM) (Model FEI TECNAI G^2 T20) operated at 200 kV. The sample

preparation for TEM involves dispersion of small amount of powder in acetone/ethanol followed by 10-20 min of ultrasonication to produce agglomeration-free suspension. After sonicating the solution, a single drop was placed on a copper grid. For microstructural characterization, the samples were mechanically polished by following the standard metallographic steps and were subsequently etched in the dilute aqua regia solution (hydrochloric acid and nitric acid in a 3:1 molar ratio). The microstructures were examined using a Scanning Electron Microscope (SEM) (Model: FEI, Quanta 200F and ZEISS, EVO) operated at 30 kV and 20 kV and equipped with EDS detector. The absolute density of the SPSed sample was measured by following the Archimedes principle using distilled water as a medium. Thermal stability of SPS-prepared alloy was studied by differential scanning calorimetry (DSC-404-F3 Pegasus, Netzsch) with suitable heat treatments. The mechanical response of the samples in the SPSed and heat-treated conditions were evaluated through microhardness instrumented indentation tester (MHT^3, Anton Paar) at a load of 500 mN with the loading and unloading rate of 1000 mN/min. The indents were observed through the optical microscope retrofitted with the instrument are given in **Fig. S3**. Minimum of ten measurements were done to calculate the average microhardness value. The hardness of the samples were computed through Oliver-Pharr method [37].

2.2. Machine-learning and CALPHAD predictions

For machine-learning predictions, a pre-trained model [38] was used to calculate the phase fractions of FCC, BCC and Intermetallic (IM) phases. This model comprises a neural-network ensemble that takes 14 alloy features as input to predict phase fractions, and it has been shown to predict phase fractions accurately in a variety of HEAs [38]. CALPHAD calculations were performed using Thermo-Calc with TCHEA5 database that has been developed for HEAs.

2.3. DFT and Short-Range Order

The DFT-based Korringa-Kohn-Rostoker (KKR) method (a Greens' function theory) combined with the coherent potential approximation (CPA) was used to calculate total energy of arbitrary solid-solution alloys [39]. The KKR-CPA performs configurational averaging over all configurations in infinite lattice simultaneously with DFT charge self-consistency, and properly includes alloy-induced Friedel impurity-charge screening. For DFT, we used the Perdew-Burke-Ernzerhof (PBE) exchange-correlation functional for solids [40]. An equally spaced *k*-space mesh of 24 × 24 × 24 was used for Brillouin-zone integrations. The core electrons were treated fully relativistically (includes spin-orbit coupling), while semi-core/valence electrons were treated scalar relativistically (i.e., neglecting spin-orbit coupling). Warren-Cowley short-range order (SRO) parameters $\alpha_{\mu\nu}^{ij}$ (μ, ν denote elemental occupations of sites i,j in a Bravais lattice) were calculated from thermodynamic linear-response theory [12, 41–44] using homogeneous alloy composition $\{c_\mu^i\}$ as a reference. For a homogeneous solid-solution alloy with $\{c_\mu^i\}$, the SRO dictates pair probabilities $P_{\mu\nu}^{ij} = c_\mu^i c_\nu^j \left(1 - \alpha_{\mu\nu}^{ij}\right)$ that

can affect chemical short-range order, as well as mechanical behaviour [45]. For a dominant **k**-space wavevector $\mathbf{k} = \mathbf{k}_{\boldsymbol{o}}$, the SRO diverges at the spinodal temperature (T_{sp}) due to absolute instability to the correlated fluctuations, which provides an estimate for SRO and the order-disorder or miscibility temperature [12]. This first-principles theory of SRO is based on the electronic structure of the alloy; therefore, it directly embodies underlying electronic and alloying effects (like band-filling, hybridization, or Fermi-surface nesting [46].

3. Results and discussion

3.1. Machine-learning and CALPHAD predictions

A pre-trained ML model [38], built for as-cast alloys, was used for a preliminary probe into the phase evolution starting with equiatomic CrFeCoNi as the base composition and we calculated the effect of separate or simultaneous addition of Al and Zn. **Figure 1(a-d)** shows FCC, BCC and IM phase fractions predicted. $Al_x(CoCrFeNi)_{1-x}$ has been extensively studied [17,18] and the model predictions (**Fig. 1a**) match the reported transition from FCC to BCC structure with Al addition. The model predicts significant IM formation with addition of Zn to CrFeCoNi (**Fig. 1b**), which could be due to the elemental segregation promoted by Zn as it has a strong tendency to cluster with Cr and Fe; this is supported by large positive values of Miedema's chemical enthalpy of mixing for Zn-Cr and Zn-Fe binary pairs in **Fig. 1e**. Addition of Al to CrFeCoNiZn is predicted to further increase the IM formation (**Fig. 1c**), indicating that Al further promotes the elemental segregation caused by Zn. One can also observe that increasing Al content results in an increase in BCC phase fraction, which is similar (albeit to a lower extent) as experimental observations in the AlCrFeCoNi system. Addition of Zn to AlCrFeCoNi (which has single-phase BCC structure) is predicted to initiate the formation of a new FCC phase at low Zn content up to 3 at.% (**Fig. 1d**). With further Zn addition, the FCC phase fraction is predicted to remain fairly constant (approximately 20%) while the BCC phase is predicted to dissociate resulting in formation of a significant amount of IM phases, along with BCC and FCC phases, in equiatomic AlCrFeCoNiZn. This is intriguing as this provides us with insights that Zn-doped AlCrFeCoNi alloys may actually have significantly higher hardness due to the presence of a large amount of IM(s) as well as a BCC phase that should have a smaller number of slip systems as compared to the FCC phase – which we have tested experimentally and presented below in this section. In short, the ML model provides two key predictions – firstly, Zn in CrFeCoNi will cause significant IM formation and, secondly, combined Al with Zn will further promote the IM formation.

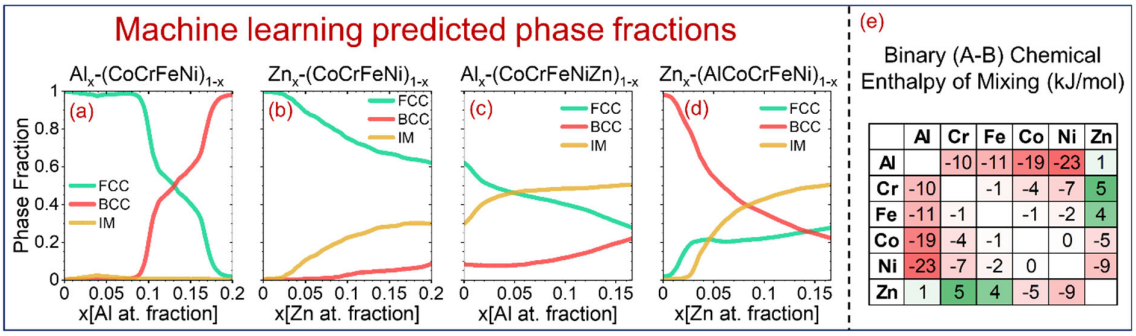

	Al	Cr	Fe	Co	Ni	Zn
Al		-10	-11	-19	-23	1
Cr	-10		-1	-4	-7	5
Fe	-11	-1		-1	-2	4
Co	-19	-4	-1		0	-5
Ni	-23	-7	-2	0		-9
Zn	1	5	4	-5	-9	

Fig. 1. FCC, BCC and Intermetallic (IM) phase fractions predicted by pre-trained ML model in **(a)** Al$_x$-(CoCrFeNi)$_{1-x}$, **(b)** Zn$_x$-(CoCrFeNi)$_{1-x}$, **(c)** Al$_x$-(CoCrFeNiZn)$_{1-x}$, and **(d)** Zn$_x$-(AlCoCrFeNi)$_{1-x}$ alloy systems. **(e)** Miedema's chemical enthalpy of mixing for binary pairs in solid-solution phase.

While the ML model [38] is capable of probing phase fractions along compositional variations, it cannot predict – **a)** the effect of temperature as it was built for as-cast alloys at room temperature, and **b)** the elemental composition of individual phases. Because the alloy samples are prepared using SPS and are also heat-treated later, we used CALPHAD to predict the effect of temperature on the composition and transition of phases. **Figure 2** shows the CALPHAD predictions for AlCrFeCoNiZn. The key predictions from these results are: **a)** the entire Zn content in the alloy segregates with Ni to form a $Zn_{3.55}Ni$ intermetallic (GAMMA_D83, structure type – Cu_9Al_4, **Fig. 2f**), which is stable from room temperature to its melting point of 780°C; **b)** formation of separate Cr-rich (BCC_B2#1, **Fig. 2b**) and Fe-rich (BCC_B2#3, **Fig. 2d**) phases that remain stable from room temperature to 542°C, where they combine to form a (Cr, Fe)-rich σ phase (SIGMA, **Fig. 2g**) that remains stable up to 852°C; and **c)** entire Al content in the alloy segregates into (BCC/B2)-type phases (BCC_B2#2 & BCC_B2#4, **Fig. 2(c, e)**), which are almost Cr- and Zn-free. We note that in AlCrFeCoNi (**Fig. S1**), where Zn is not present, CALPHAD does not predict formation of (Fe, Co)-rich BCC/B2 phase. The exceptional tendency of Zn to preferentially segregate with Ni might be a driver for this behavior as formation of (Zn, Ni)-rich intermetallic would deplete Ni in the BCC/B2 phase; and as Ni is a high VEC element, Fe and Co (with lower VEC than Ni) might segregate to maintain the stability of primary BCC/B2 phase that has Al. In effect, the comparison between CALPHAD predictions for AlCrFeCoNi and AlCrFeCoNiZn suggests that Zn might segregate almost exclusively with Ni and a (Fe, Co)-rich might form in AlCrFeCoNiZn. While these calculations give needed insights, it is important to be mindful of two discrepancies in these CALPHAD predictions – **a)** almost pure Cr is predicted as a separate phase (BCC_B2#1, **Fig. 2b**) but such behavior has not been reported in any experimental or *ab initio* studies, and **b)** partial melting of AlCrFeCoNiZn is predicted to start at 780°C, but no melting was observed in the sample during heat treatment at 900°C or in DSC thermogram in this temperature range (i.e., under 1100°C). This also highlights a key challenge in the modelling of HEAs that arises due to the astronomically large compositional space that has to be probed with relatively scarce data as compared to traditional alloys. One

way to address this is by borrowing the best from different models. While ML models excel at determining the as-cast phase selection and properties at room temperature [38,47–49], CALPHAD is often more reliable at high temperatures. While DFT calculations are unmatched in their accuracy and reliability, ML and CALPHAD offer vastly better high-throughput capabilities. Thus, rather than relying on a single technique, we have implemented multiple modeling tools here to identify relative consistencies across the techniques.

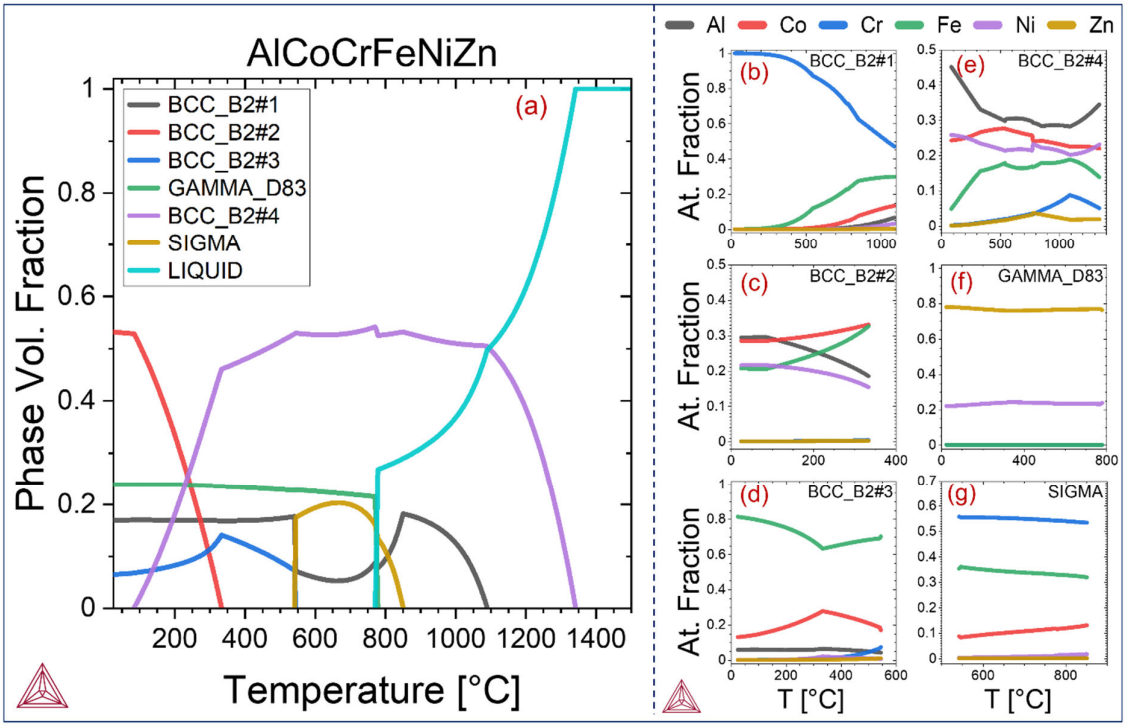

Fig. 2. CALPHAD predictions for phase transitions and phase compositions versus temperature in AlCrFeCoNiZn. **(a)** Volume fraction of phases as a function of temperature. **(b-g)** Elemental composition of each phase as a function of temperature over the temperature range where it is stable.

3.2. Characterization using X-ray Diffraction

The diffraction patterns of milled AlCrFeCoNiZn powder at different milling durations are shown in **Fig. 3a**. At the start of milling process (after 10 mins), peaks corresponding to all constituent elements were observed. As milling proceeds for 10h, the peaks broadened and the intensity of most peaks decreased significantly, confirming alloying of the elements to a significant extent. With increased milling time, a single-phase BCC structure was observed after 20h. The milling time was further increased to 30h to see whether there is any further phase change in the alloy. However, no noticeable difference was observed except for an increase in the broadening of the peaks. The 30h-milled powder showed formation of a single-phase BCC structure and **Fig. 3b** shows the full pattern Rietveld refinement. The refined lattice parameter of the 30h-milled powder of the BCC phase was calculated to be 2.885 Å. The nanocrystalline nature of milled powder was confirmed through

TEM. **Figure 3c** shows the bright-field image contains nanostructured grains. The formation of ring pattern (inset image) in selected area electron diffraction (SAED) pattern suggests the polycrystalline nature of the 30h-milled powder with single-phase BCC structure, corroborating the XRD findings. The dark-field TEM image (**Fig. 3d**) was captured using a (110) ring, showing the diffracted nanocrystals. The representative image shows the presence of crystals of different sizes (approximately 25-40 nm) that leads to the variations in intensity observed in the (110) ring of SADP.

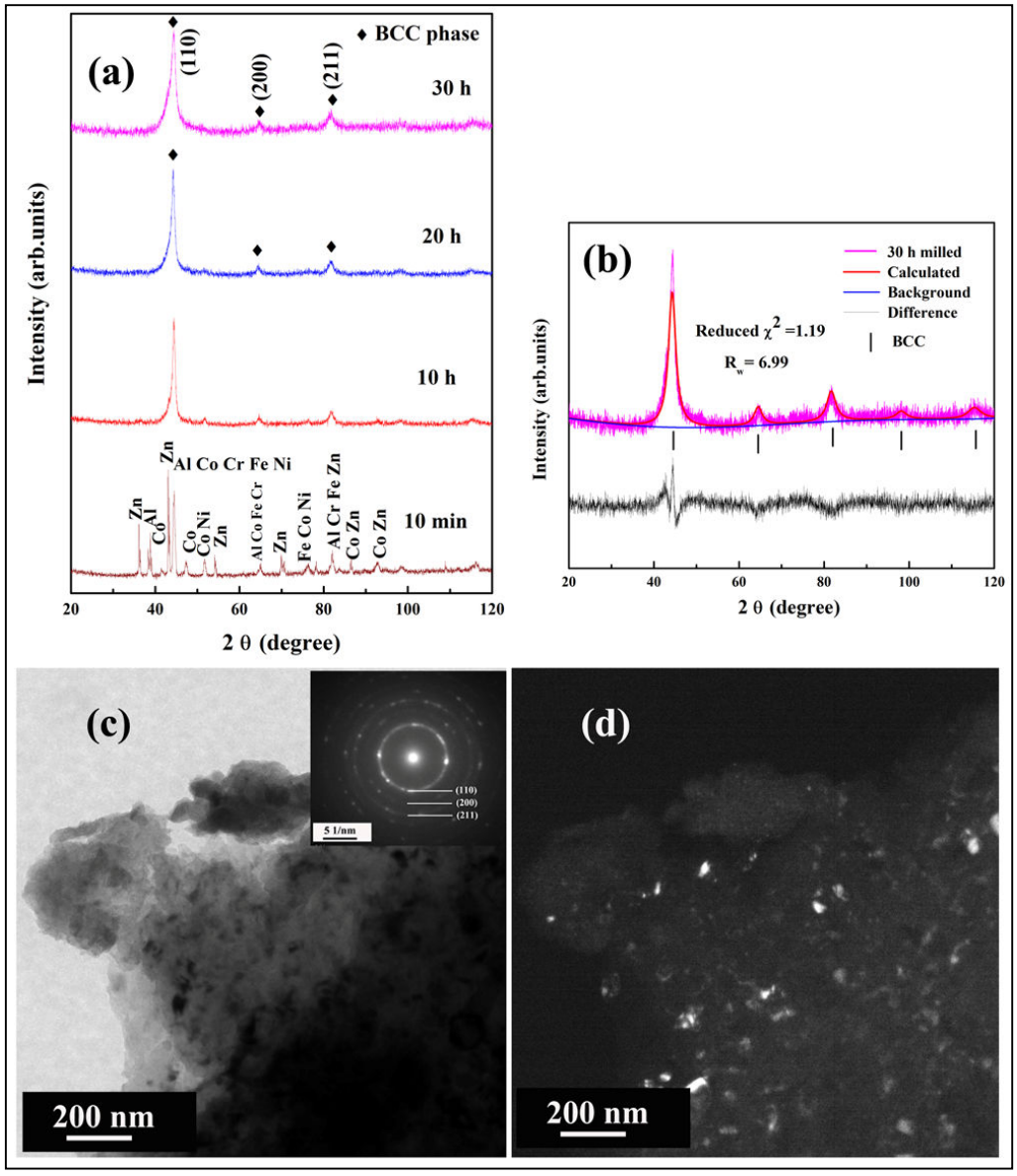

Fig. 3. Structure evolution during milling process. (a) X-ray diffraction patterns of AlCrFeCoNiZn HEA powder milled up to 30h. The evolution of the single-phase BCC structure is discerned, **(b)** full pattern refinement of 30h milled powder sample, **(c)** TEM bright-field image (inset gives the SADP), **(d)** dark field image of 30 hour milled sample.

Figure 4a shows the diffraction pattern of SPS-prepared AlCrFeCoNiZn at 800°C. Single-phase BCC structure of the alloy was observed even after sintering. The Rietveld refined pattern of the SPSed sample is given in **Fig. 4b** and the refined value of the lattice parameter turns out to be 2.883 Å. While we see phase separation in EDS data for SPS-prepared alloy, the peaks for these phases appear to have been masked by the background in the XRD pattern owing to their low volume fractions. The absolute density of the sintered alloy, measured by Archimedes principle is 6.40 g/cc against the rule of mixture density of 7.11 g/cc. The sintered pellets appeared dense and no visible porosity was observed in the SEM images. The DSC thermogram of the SPSed sample heated up to 1300°C (**Fig. 4c**) shows no sharp reaction up to 1000°C. A small change in heat-transient in the temperature range of 80-120°C is possibly related to the release of the residual strain in the sample accumulated during milling. The broad temperature range (200 to 1000°C) of thermal events in the DSC thermogram indicates that the formation of the different phases (presumably (Al, Cr)-rich and (Fe, Co)-rich phases) is diffusion-controlled and occurs gradually. The same was confirmed via subsequent heat treatments at different temperatures and cooling conditions.

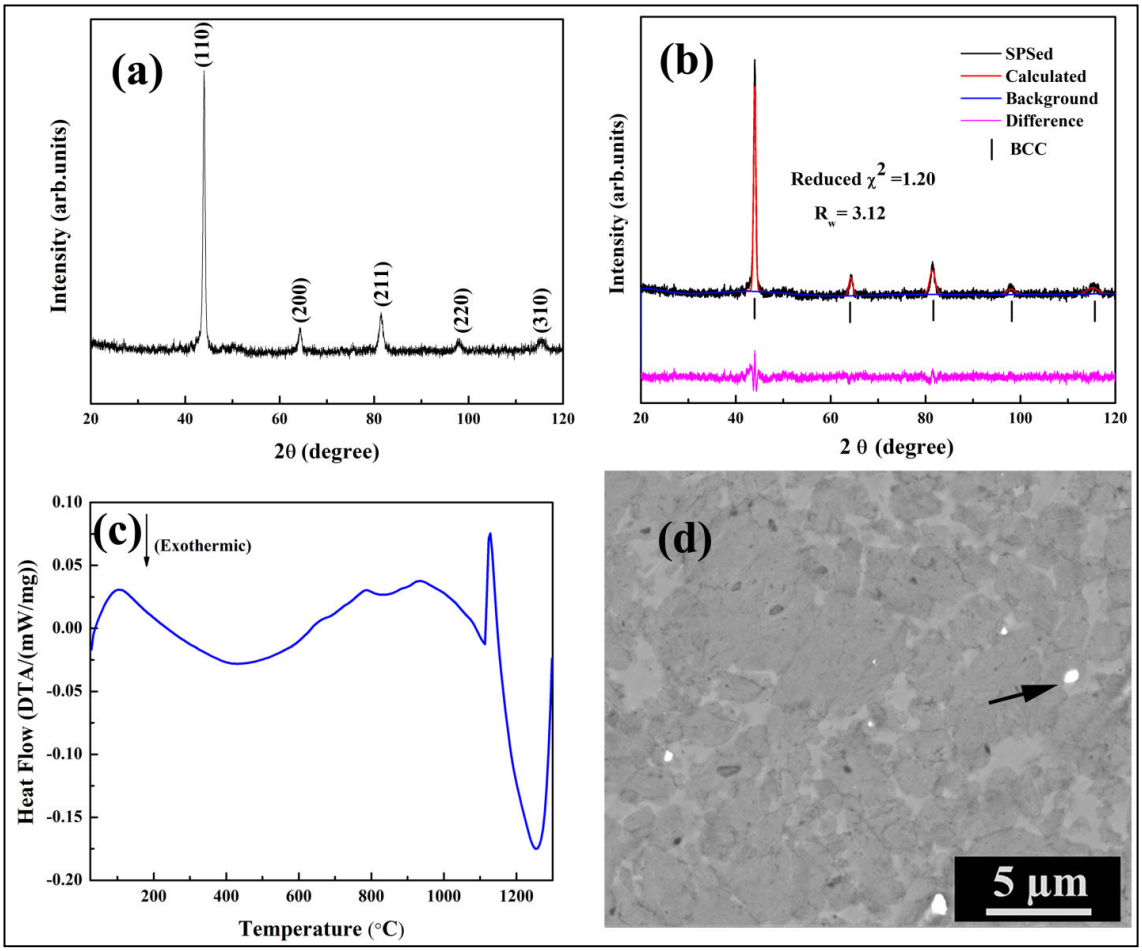

Fig. 4. Structure and thermal stability of SPS-prepared AlCrFeCoNi alloy. (a) X-ray diffraction pattern of SPSed AlCrFeCoNiZn HEA sintered at 800°C, **(b)** full pattern refinement of SPSed sample, **(c)** the DSC thermogram of the SPSed sample heated up to 1300°C, **(d)** SEM micrograph of the SPSed sample (arrow shows the alumina particle).

The SPS-prepared alloy was further subjected to three different heat-treatment schedules – **(a)** 800°C for 2h followed by water quenching, **(b)** 900°C for 2h followed by water quenching, and **(c)** 900°C for 12h followed by furnace cooling. The diffraction pattern of the sample heat-treated at 800°C for 2h followed by water quenching (**Fig. 5a**) shows that new phases have formed along with the BCC phase. Careful indexing of the diffraction pattern confirms the formation of BCC phase along with the sigma-type phase. The sample heat-treated at 900°C shows the BCC and sigma-type phases along with the evolution of FCC phase (**Fig. 5b**).

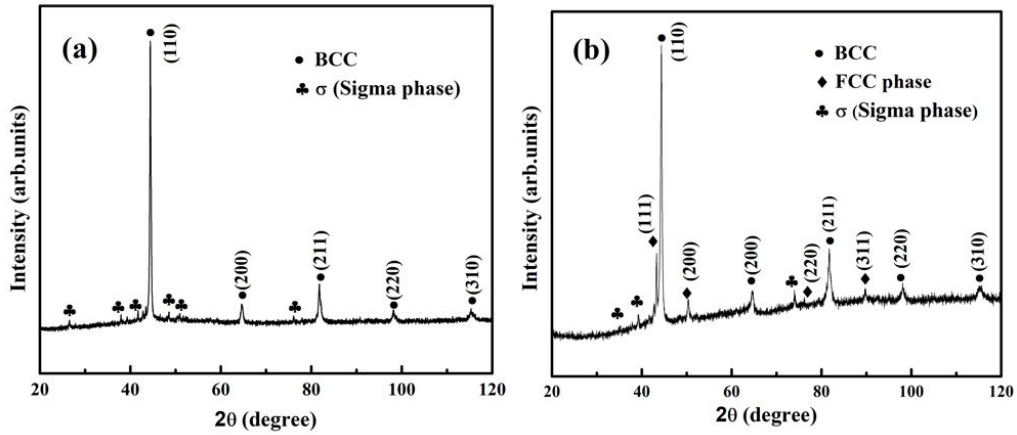

Fig. 5. The X-ray diffraction pattern of SPSed AlCrFeCoNiZn HEA sample heat-treated at (a) 800°C and **(b)** 900°C for 2 h, followed by water quenching. The formation of BCC, FCC and sigma-type phase could be discerned.

To understand the stability of these evolved phases, another sample was heat-treated at 900°C for 12h followed by furnace cooling to drive the system towards equilibrium. The XRD pattern (Fig. 6) shows the formation of Ni-Al type B2 (a= 2.86± 0.01Å), FCC (a= 3.59 ± 0.02Å) and sigma-type phase. We also looked at the diffraction plots of heat-treated samples at 900 and 1100°C for 2h in Co-target to get the better intensity plots (Fig. 7) of evolved phase. The sample of 900°C heat-treated conditions (a) has shown the evolution of BCC (Co-Fe type, PDF#-00-049-1567), FCC, sigma (Fe-Cr type, PDF#- 0071-7530) and Al-Cr type, PDF#-01-082-2599) phases. With increase in heat-treatment temperature of 1100°C, shows the more equilibrium phase of FCC, Ni-Zn (PDF#-01=085-7584, a= 8.93Å, cI-52)) and Al-Cr type phase. These results are in agreement with the elemental segregation maps, predicted through ML.

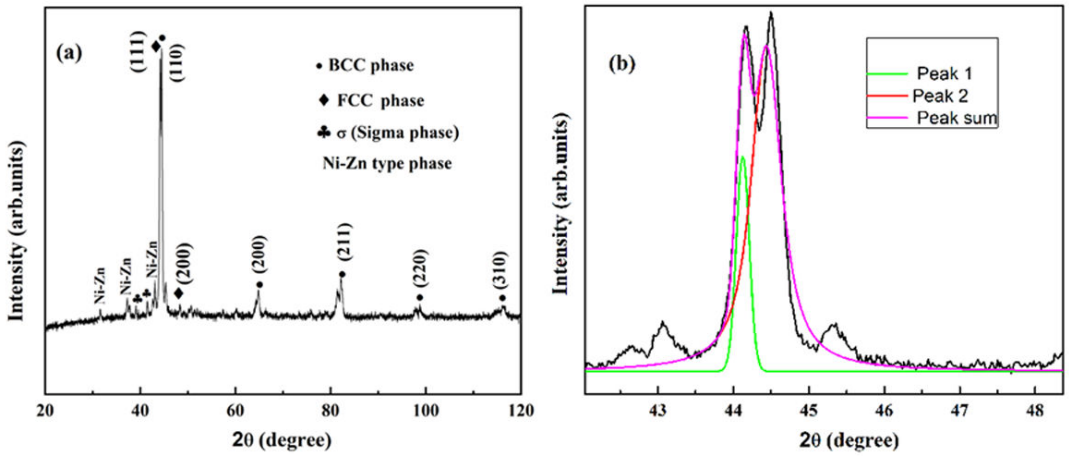

Fig. 6. (a) X-ray diffraction pattern of the SPS-prepared AlCrFeCoNi heat-treated at 900°C for 12h followed by furnace cooling. The formation of B2, FCC and sigma-type phase could be discerned along with the stable BCC phase. **(b)** Deconvolution of the major peak.

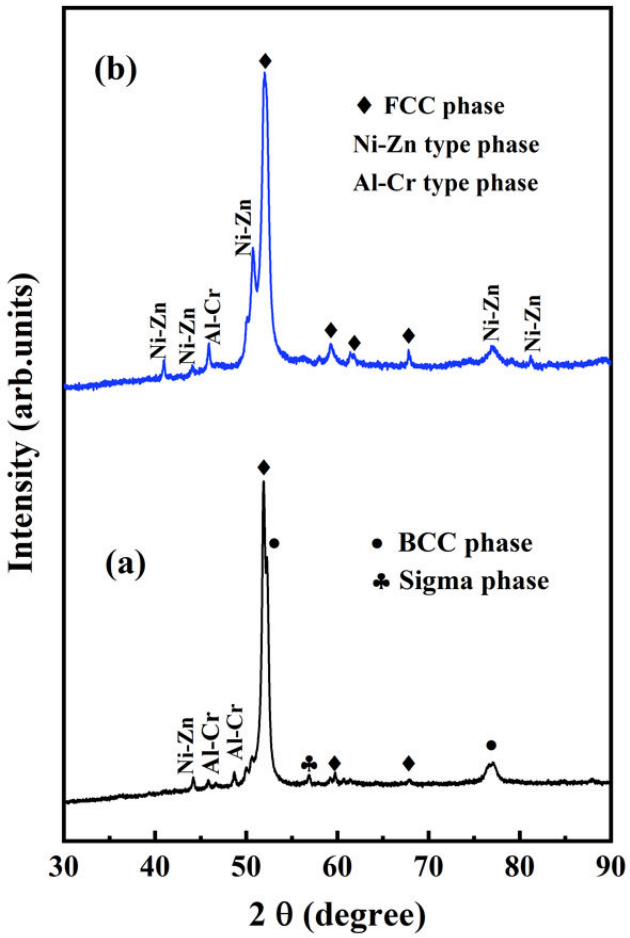

Fig.7. The X-ray diffraction plots of samples heat-treated at (a) 900°C and (b) 1100 °C for 2 h, followed by furnace cooling. The Co-target was used to get the better diffraction intensity of evolved phases.

3.3. Elemental segregation and phase separation from EDS data

The elemental maps (atomic percent) obtained from EDS were used to analyze the elemental segregation and phase separation behavior of AlCrFeCoNiZn following SPS and heat-treatments, as seen in **Fig. 8**. In SPSed sample, **Fig. 8(a, d)**, the formation of a (Fe, Co)-rich phase, with very low Al and Cr content, is clearly evident. Al & Cr also appear to segregate together to form an (Al, Cr)-rich phase. Ni and Zn don't show any significant segregation in SPSed sample, although a slightly higher and lower Ni content is associated with (Al, Cr)-rich and (Fe, Co)-rich phases, respectively. Thus, the EDS maps for SPSed sample show signs of elemental segregation that was also predicted by the ML and the CALPHAD approach. But there are two key deviations. Firstly, formation of an (Al, Cr)-rich phase is seen here which was neither predicted by the CALPHAD approach here nor has been reported in any previous studies on AlCrFeCoNi or related alloys. Secondly, the Zn segregation in SPSed sample is quite insignificant as compared to the expectations set by ML and CALPHAD approach. This prompted us to perform heat treatment studies since SPS exposes the sample to high temperature for a very brief duration that may not be sufficient to form equilibrium structures.

Heat treatment at 900°C for 2h, followed by water quenching, shows similar segregation tendencies as SPSed sample with the formation of (Al, Cr)-rich and (Fe, Co)-rich phases, as seen in **Fig. 8b**; although the size of these phases has increased after heat treatment, as seen in **Fig. 8e**. Also, we see that Zn and Ni have started segregating together to form (Zn, Ni)-rich regions, although the extent of Zn segregation is still not too significant. Prolonged heat treatment at 900°C for 12h, followed by furnace cooling, makes the elemental segregation significantly pronounced even though the nature of segregation remains the same, as seen in **Fig. 8c**. The size and volume of (Al, Cr)-rich phase increases considerably, as seen in **Fig. 8f**, along with its Al & Cr content, resulting in large regions that are depleted in Al and Cr. On the other hand, there is no significant change in the (Fe, Co)-rich phase. With prolonged heat treatment, Zn and Ni have segregated together to form a phase that contains appreciable Co and Fe but very low Al and Cr, as seen in **Fig. 8c**. At the same time, (Al, Cr)-rich and (Fe, Co)-rich phases have been considerably depleted of Ni and Zn.

In brief, the heat treatment leads to elemental segregation resulting in the separation of system into three primary phases: (Zn, Ni)-rich, (Al, Cr)-rich and (Fe, Co)-rich phase. The phase-segmented microstructures of SPSed and heat-treated alloys have been shown in **Fig. 8(d-f)**. Since (Al, Cr)-rich phase has not been reported in any other studies on (AlCoCrFeNi)-based alloys, its formation here could be attributed to the presence of Zn which has a strong clustering tendency with respect to Cr.

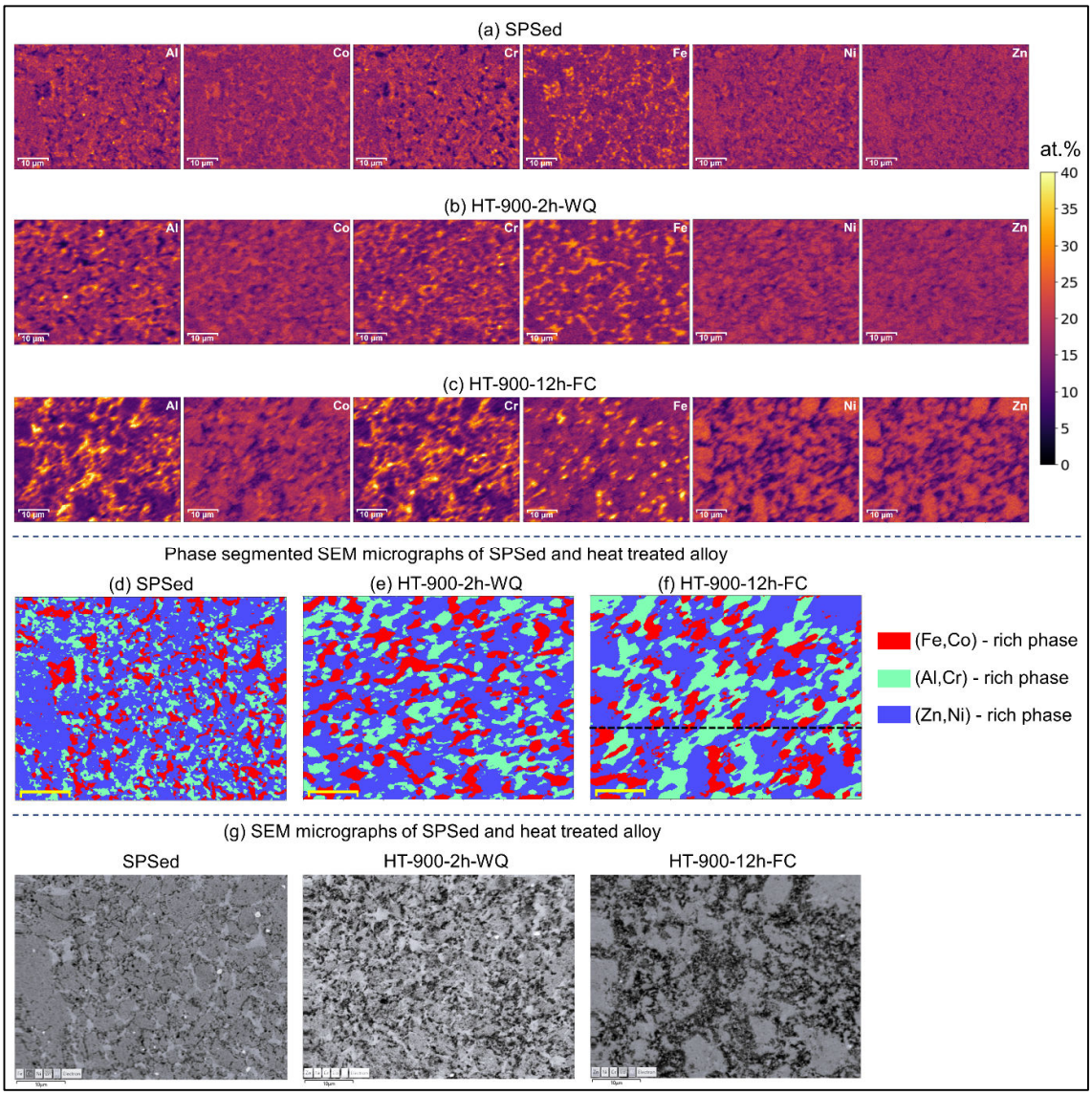

Fig. 8. Elemental segregation and phase separation from Energy Dispersive Spectroscopy data. Element maps (atomic percent) for **(a)** SPSed, **(b)** HT-900-2h-WQ, and **(c)** HT-900-12h-FC samples. Phase segmented microstructures of **(d)** SPSed, **(e)** HT-900-2h-WQ, and **(f)** HT-900-12h-FC samples. **(g)** SEM micrographs of SPSed and heat-treated samples. Here, "HT-900-2h-WQ" represents sample heat-treated at 900 °C for 2h & water quenched, "HT-900-12h-FC" represents sample heat-treated at 900 °C for 12h & furnace cooled. The black dashed line in (f) indicates the scan line profile for Fig. 8. The scale bar used throughout this figure corresponds to 10 µm length.

Further analysis of the EDS data indicates that when the sample undergoes heat treatment at 900°C for 12h followed by furnace cooling, the (Al, Cr)-rich phase might be undergoing a separation into Cr-rich and Al-rich regions, as seen in **Fig. 9**. The line scan indicates that this separation might be occurring over ~ 1 µm distances (**Fig. 9c)**, but the spatial resolution of EDS maps here is not sufficient to make conclusive claims about the exact nature of this behavior. Future studies into this behavior may lead to more insights.

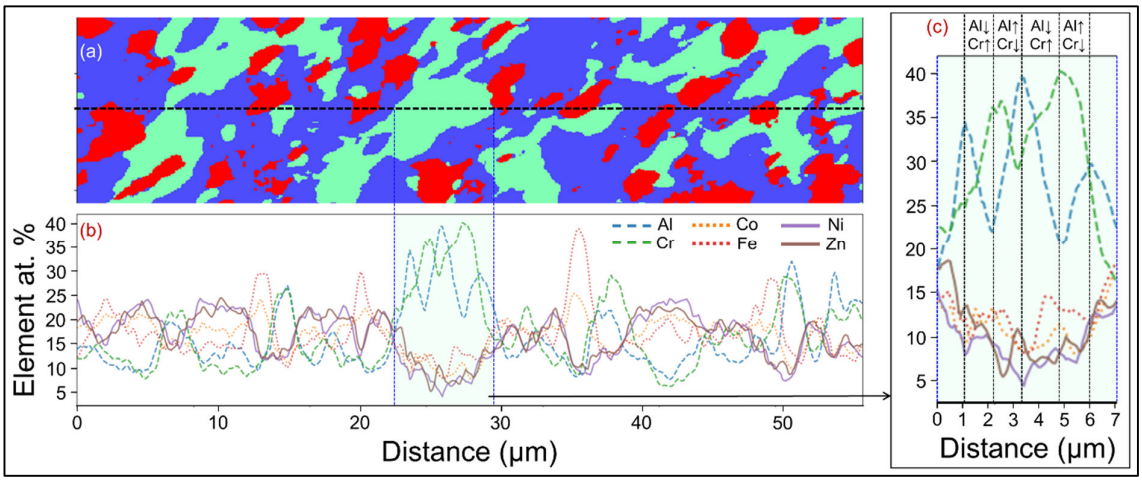

Fig. 9. Line scan to probe phase separation within (Al, Cr)-rich phase in annealed sample (900 °C-12h-furnace cooled). **(a)** Scan line profile in the segmented microstructure. **(b)** Elemental distribution (atomic percent) plot along the scan line. **(c)** Magnified view of region highlighted in (b). The scan line profile is also shown in Fig. 7f.

3.4. Electronic structure of equiatomic AlCrFeCoNiZn

To understand the ML and CALPHAD predictions and the experimental results, we performed a detailed electronic-structure and thermodynamic analysis of the equiatomic AlCrFeCoNiZn alloy. The partial density of states (PDOS) of AlCrFeCoNiZn was compared in bcc and fcc phases. Singh et al. [12] have discussed the rules of solid-solution formation, where the energy of formation (E_{form}) range is $-11 \lesssim E_{form} \lesssim 5$ mRy (per atom). The E_{form} for BCC AlCrFeCoNiZn is +5.48 mRy/atom close to solid-solution formation range, while VEC (8.0) is much higher for bcc formation ($4 < VEC < 6.7$). In contrast, E_{form} of +7.71 mRy/atom in the FCC phase is higher for solid-solution phase formation, however, VEC (8.0) is just on the edge of FCC formation ($VEC > 8.0$). Recently, for MPEAs [41] the *d*-band filling and hybridization was shown to play significant role in driving single-phase (BCC or FCC) stability. The higher positive E_{form} of FCC AlCrFeCoNiZn possibly restricts formation of single-phase alloy by reducing the number of unlike bonding pairs required for improved phase stability. The competing E_{form} and VEC in FCC and BCC phase can lead to energy instability of single-phase AlCrFeCoNiZn. However, the underlying thermodynamic and electronic reasons for this behaviour are not obvious.

To understand the electronic origin, we plot partial (electronic) density of states (DOS) for of AlCrFeCoNiZn in **Fig. 10**. The BCC phase in **Fig. 10a** shows strong hybridized states near -0.08 Ry in the majority (up-spin) channel below the Fermi energy (E_{Fermi}) compared to FCC phase (**Fig. 10b**). The reduced hybridization in BCC phase increases the filling of bonding states below E_{Fermi}; at the same time, it pushes antibonding (or nonbonding) states above E_{Fermi}. For the FCC phase (**Fig. 10b**), we found strong disorder broadening that leads to weak hybridization and reduces the ordering strength. Both BCC (+5.48 mRy/atom) and FCC (+7.71 mRy/atom) phases show positive E_{form}, i.e., FCC is energetically higher by

+2.23 mRy/atom. If we look closely at partial DOS in minority (down-spin) channel, FCC phase in **Fig. 10b** has disorder broadened Co-*3d* peak at E_{Fermi}, while the same peak is slightly away from E_{Fermi} in BCC phase. The Co-*3d* gains more charges in FCC vs BCC phase that pushes the Co-3*d* to E_{Fermi} and enhances the energy instability.

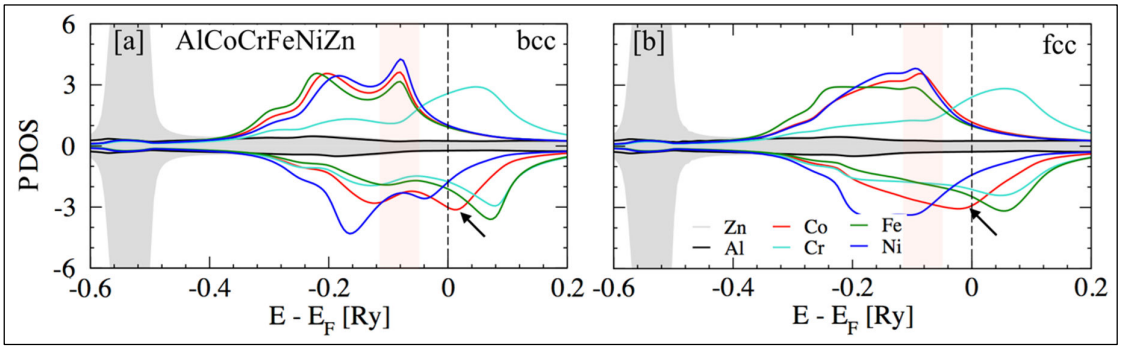

Fig.10. DFT partial density of states in **(a)** bcc, and **(b)** fcc phases for AlCrFeCoNiZn HEA.

We also assessed the SRO in FCC AlCrFeCoNiZn to understand the change in probability distribution of each element on sublattices of $L1_2$ phase, compared to disordered phase. The SRO analysis suggests that Cr-Fe-Zn and Al-Ni-Co preferably go, respectively, to 1a (000) and 3c (0 ½ ½) positions in the $L1_2$ phase. This explains the phase stability in this system as E_{form} in $L1_2$ phase is -0.55 mRy/atom, lower than both BCC (+5.48 mRy/atom) and FCC (7.71 mRy/atom). Formation enthalpy alone does not explain the kinetically slow diffusion transformation to $L1_2$ phase from BCC precursors [50], however, the low {111} stacking-fault energies besides the large free-energy barrier are known to enable such transformations [51]. The stacking-fault energy (SFE) in the FCC phase of AlCrFeCoNiZn is 5.4 mJ/m^2; interestingly, a low SFE supports the kinetically slow diffusion transformation formation of $L1_2$ phase.

In contrast, a positive formation enthalpy (+5.48 mRy/atom) for BCC AlCrFeCoNiZn suggests weak thermodynamic stability, while strong hybridization in **Fig. 10 a** shows tendency of ordering interaction in BCC phase. Moreover, experiments in **Fig. 8** found (Zn, Ni)-rich, (Al, Cr)-rich and (Fe, Co)-rich phases that suggests that certain elements lead to increased chemical interactions in BCC phase. We also found this behaviour through increased hybridization in partial DOS analysis in **Fig. 10a**. To understand this better, we plot temperature dependence of Warren-Cowley parameters in **Fig. 11**, which is a thermodynamic representation of increased interactions due to infinitesimal change in local chemical concentration fluctuations, i.e., SRO [12,41–44].

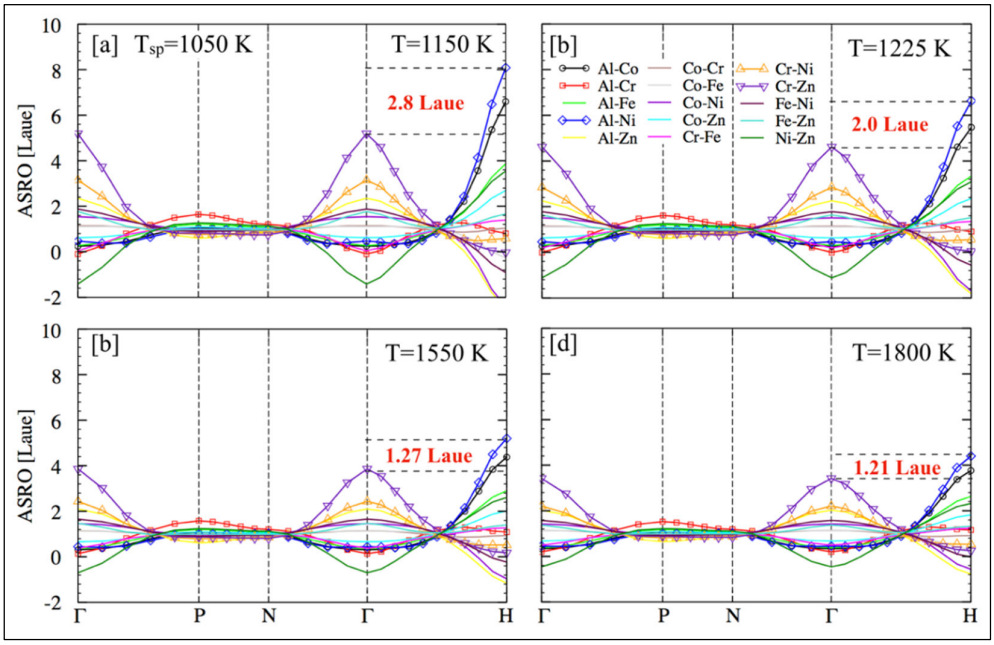

Fig. 11. Warren-Cowley SRO parameters $[\alpha_{\mu\nu}(k;T)]$ in Laue units for AlCrFeCoNiZn plotted above the spinodal temperature (Tsp ~ 1050 K) at **(a)** 1150 K, **(b)** 1225 K, **(c)** 1550 K, and **(d)** 1800 K. The SRO is plotted along BCC high-symmetry Brillouin zone directions.

The SRO in **Fig. 11** shows peak at H [111] point, with Al-Ni as dominant pair in AlCrFeCoNiZn. Interestingly, the Al-Ni pair with peak at H point in **Fig. 11b** is the most dominant SRO mode that shows the ordering (B2-type) interaction. The dominant SRO pairs reveals the unstable (Fourier) modes with ordering wavevector (k_o) or phase-separation (clustering at k_o = (000)) at spinodal temperature (T_{sp}~1050 K) [12,41–44]. Despite decreasing SRO strength of Al-Ni pair from 2.80 Laue at 1150 K to 1.21 Laue at 1800 K, the Al-Ni pair remains dominant at all temperatures. Interestingly, we also found stronger and competing clustering pairs (Cr-Zn and Cr-Ni) with peak at Γ (=000) at higher temperatures, suggesting that energetically Cr does not prefer to sit in the neighborhood of Zn/Ni. Therefore, if the opportunity arises, Cr will phase separate with both Ni and Zn. This is further affirmed through clustering tendency of Cr-Ni/Cr-Zn pairs (with peak at the Γ point) and ordering tendency of Ni-Zn (with peak at hte *H* point), as shown in **Fig. 11**. This finding is in agreement with our experiments in **Fig. 8(d-f)** that shows formation of (Zn, Ni)-rich phases. Moreover, the peak in DSC measurements at 1063 K, where some of the decompositions occur, is very close to our predicted spinodal temperature (1050 K).

3.5. Mechanical Response of AlCrFeCoNiZn

The mechanical response of SPS-prepared and heat-treated samples was studied using the Vickers microhardness-instrumented indentation technique. The plots of the applied load and depth of penetration have been shown in **Fig. 12**. The hardness and elastic modulus (E) for the SPS-prepared sample was measured as ~ 8.81 GPa and 149 GPa, respectively. Upon

heat-treatment at 800℃ and 900℃ for 2h, the hardness decreased to ~ 8.77 GPa and ~ 8.50 GPa, respectively, whereas the elastic modulus increased to 163 GPa and 182 GPa, respectively, reflecting the changes in phase compositions. The sample heat-treated at 900℃ for 12h followed by furnace cooling yielded a hardness of ~ 8.24 GPa with an elastic modulus of ~185 GPa. The alloy's yield strength was estimated using Tabor's equation, $\sigma_y = H_v/3$; where σ_y is yield-strength (GPa), and H_v is the hardness (GPa). The results of hardness (Hv), elastic modulus (E) and yield strength (σ_y) are summarized in **Table 1**. No indentation cracks were observed in the micrographs, as seen in **Fig. S3**. The higher hardness values in the SPSed and heat-treated samples are the resultant of the nanostructured grains formation and precipitation of intermetallic compounds of (Al, Cr)-rich, (Fe, Co) rich and (Zn, Ni)-rich phases, respectively.

Table 1: Microhardness, elastic modulus and estimated yield strength of consolidated AlCrFeCoNiZn HEA at different conditions

Sample Condition	Microhardness (H_v) (GPa) Load- 5000 mN	Elastic Modulus (E) (GPa)	Estimated Yield Strength (σ_y) (GPa)
SPS-prepared	8.81	149	2.93
SPSed+ Annealed at 800°C for 2 h-water quenched	8.77	163	2.92
SPSed+ Annealed at 900°C for 2 h-water quenched	8.50	182	2.83
SPSed+ Annealed at 900°C for 12 h-furnace cooled	8.24	185	2.74

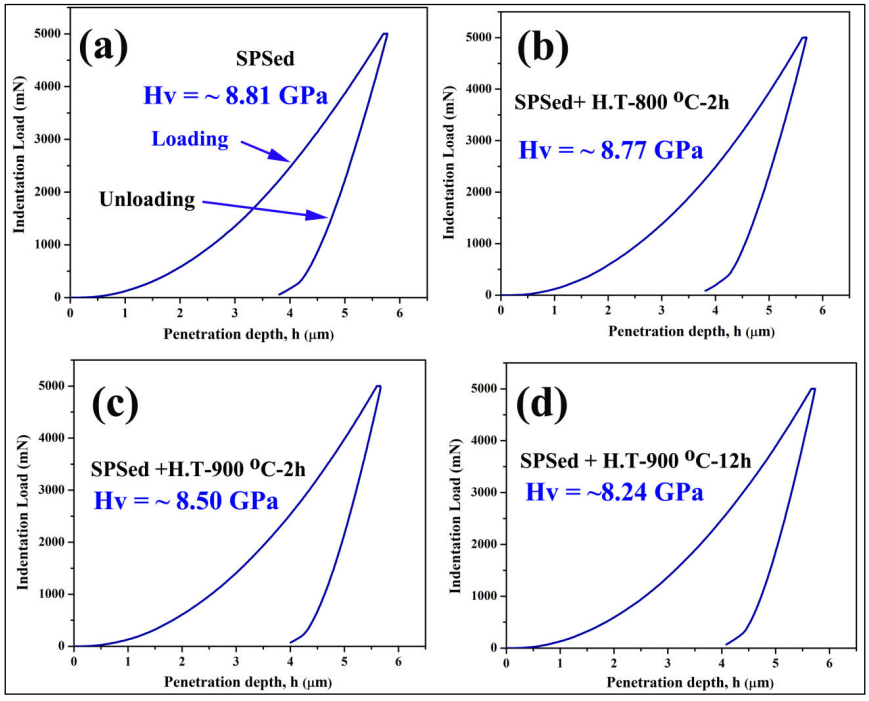

Fig. 12. Load (mN) versus penetration depth (μm) plots of AlCrFeCoNiZn for: **(a)** as-SPS-prepared, **(b)** heat-treated at 800°C followed by water quenching, **(c)** heat treated at 900°C for 2h followed by water quenching, and **(d)** heat-treated at 900°C for 12h followed by furnace cooling. Corresponding values of hardness (Hv) is given in the respective plots.

4. Conclusions

While Al addition is known to cause transition from FCC to BCC in $Al_x(CoCrFeNi)_{1-x}$ (owing to considerable reduction in VEC), the addition of Zn to AlCrFeCoNi poses exciting and open questions as to how it would affect the phase evolution. The Zn has a high VEC that should stabilize FCC phase, while it exhibits ordering tendency with Ni and Co and strong clustering tendency with Cr & Fe, thereby hinting towards phase separation. To address these questions, we probed the phase evolution in AlCrFeCoNiZn using a combination of experimental (XRD, SEM, EDS and DSC) and computational (machine learning, CALPHAD and DFT) techniques. It is important to understand that phase evolution in high entropy chemically complex system is a problem that is still being probed scientifically and that a combination of techniques rather than a single modeling approach is required to gain a deeper understanding of the system.

To conclude, we find that:

(a) A strong clustering tendency of (Cr-Zn) and (Cr-Ni) pairs, combined with the strong ordering of (Zn-Ni) pair, drives out the Cr that in turn combines with Al to form an (Al-Cr)-rich phase. This study reports formation of (Al, Cr)-rich phases in (AlCrFeCoNi)-based HEAs that usually end up with (Al, Ni)-rich phases or intermetallics due to the strong ordering tendency of (Al-Ni) pair that is disturbed due to the presence of Zn.

(b) The AI/ML model accurately predicts the tendency of intermetallic phase formation, however, the lack of training data for intermetallic type prevents from identifying the ordering phases. On the other hand, we attribute the erroneous CALPHAD predictions to the lack of a well-assessed database for Zn-HEAs.

(c) The mechanically alloyed AlCrFeCoNiZn HEA powder shows single phase BCC structure. However, sintering and subsequent heat treatments lead to phase separation resulting in formation of (Al, Cr)-rich, (Fe, Co)-rich and (Zn, Ni)-rich phases.

(d) Phase separation observed in AlCrFeCoNiZn upon heat treatment is diffusion-controlled and occurs because of gradual elemental segregation as no sharp phase-transition peaks were observed in the DSC from room temperature to 1000°C.

(e) The thermodynamic stability of $L1_2$ phase arises from a considerably lower formation energy when Cr-Fe-Zn and Al-Ni-Co preferably goes to 1a (000) and 3c (0 ½ ½) positions, respectively. The kinetically slow-diffusion transformation to $L1_2$ phase from BCC precursors is made possible by the small stacking-fault energy of AlCrFeCoNiZn.

The slow diffusion-controlled transformation leading to formation of (Al, Cr)-rich phase may possibly be linked to the solute-drag effect induced by the addition of Zn; similar to how the addition of Sn slows the growth kinetics in FeCoNiCuSn alloy [52]. A similar effect has also been seen in Al-CrFeNi alloys wherein relatively small changes in Al solute concentration result in different diffusion and growth behavior [53]. Future studies are required to ascertain the exact nature of this behavior.

Acknowledgement

V.S. and N.K.M. would like to acknowledge Prof. R. K. Mandal, Dr. R. Manna, Dr. V.C. Srivastava and Dr. Joysurya Basu for useful discussion and help during the experimental investigations. V.S. also acknowledges support from IIT Ropar in the form of an institute post-doctoral fellowship. P.K.R. acknowledges support from IIT Ropar's ISIRD-II program. The theoretical work (including DFT-based methods in HEAs) at Ames Laboratory was supported by U.S. Department of Energy (DOE), Office of Science, Basic Energy Sciences, Materials Science & Engineering Division. Ames Laboratory operated by Iowa State University for the U.S. DOE under contract DE-AC02-07CH11358.

Declaration of Competing Interest

The authors declare that they have no known competing financial interests or personal relationships that could have appeared to influence the work reported in this paper.

Author Contributions

VS: Conceptualization, alloy fabrication, experimental testing and characterization, analysis of experimental results; **DB**: Machine learning calculations, analysis of EDS and CALPHAD data; **YS**: Alloy fabrication and experimental testing; **PS**: Calculations and analysis of DFT results, Review and editing; **OP:** XRD experiment; **VSH**: CALPHAD calculations, analysis of CALPHAD data; **MJK**: Supervision of XRD results, Review and editing; **GP**: Supervision of CALPHAD calculations, Review and editing; **DDJ**: Supervision of DFT calculations; Review and editing; **PKR**: Conceptualization, supervision of experimental and machine-learning work, analysis of experimental and machine-learning results, Review and editing; **NKM**: Supervision of experimental work, analysis of experimental results, Review and editing. All authors participated in writing the manuscript.

References:

[1] J.-W. Yeh, S.-K. Chen, S.-J. Lin, J.-Y. Gan, T.-S. Chin, T.-T. Shun, C.-H. Tsau, S.-Y. Chang, Nanostructured High-Entropy Alloys with Multiple Principal Elements: Novel Alloy Design Concepts and Outcomes, Advanced Engineering Materials. 6 (2004) 299–303. https://doi.org/10.1002/adem.200300567.

[2] B. Cantor, I.T.H. Chang, P. Knight, A.J.B. Vincent, Microstructural development in equiatomic multicomponent alloys, Materials Science and Engineering: A. 375–377 (2004) 213–218. https://doi.org/10.1016/j.msea.2003.10.257.

[3] E.P. George, W.A. Curtin, C.C. Tasan, High entropy alloys: A focused review of mechanical properties and deformation mechanisms, Acta Materialia. 188 (2020) 435–474. https://doi.org/10.1016/j.actamat.2019.12.015.

[4] E.P. George, D. Raabe, R.O. Ritchie, High-entropy alloys, Nat. Rev. Mater. 4 (2019) 515–534. https://doi.org/10.1038/s41578-019-0121-4.

[5] D.B. Miracle, O.N. Senkov, A critical review of high entropy alloys and related concepts, Acta Materialia. 122 (2017) 448–511. https://doi.org/10.1016/j.actamat.2016.08.081.

[6] B.S. Murty, J.W. Yeh, S. Ranganathan, P.P. Bhattacharjee, High-Entropy Alloys, 2nd ed., Elsevier, 2020. https://www.elsevier.com/books/high-entropy-alloys/murty/978-0-12-816067-1 (accessed February 12, 2020).

[7] Z. Li, K.G. Pradeep, Y. Deng, D. Raabe, C.C. Tasan, Metastable high-entropy dual-phase alloys overcome the strength–ductility trade-off, Nature. 534 (2016) 227–230. https://doi.org/10.1038/nature17981.

[8] E. Ma, X. Wu, Tailoring heterogeneities in high-entropy alloys to promote strength–ductility synergy, Nat. Commun. 10 (2019) 5623. https://doi.org/10.1038/s41467-019-13311-1.

[9] S. Wei, F. He, C.C. Tasan, Metastability in high-entropy alloys: A review, Journal of Materials Research. 33 (2018) 2924–2937. https://doi.org/10.1557/jmr.2018.306.

[10] H. Huang, Y. Wu, J. He, H. Wang, X. Liu, K. An, W. Wu, Z. Lu, Phase-Transformation Ductilization of Brittle High-Entropy Alloys via Metastability Engineering, Advanced Materials. 29 (2017) 1701678. https://doi.org/10.1002/adma.201701678.

[11] Y.F. Ye, Q. Wang, J. Lu, C.T. Liu, Y. Yang, High-entropy alloy: challenges and prospects, Materials Today. 19 (2016) 349–362. https://doi.org/10.1016/j.mattod.2015.11.026.

[12] P. Singh, A. Sharma, A.V. Smirnov, M.S. Diallo, P.K. Ray, G. Balasubramanian, D.D. Johnson, Design of high-strength refractory complex solid-solution alloys, Npj Comput. Mater. 4 (2018) 1–8. https://doi.org/10.1038/s41524-018-0072-0.

[13] F. He, Z. Wang, Q. Wu, J. Li, J. Wang, C.T. Liu, Phase separation of metastable CoCrFeNi high entropy alloy at intermediate temperatures, Scripta Materialia. 126 (2017) 15–19. https://doi.org/10.1016/j.scriptamat.2016.08.008.

[14] S. Yang, J. Lu, F. Xing, L. Zhang, Y. Zhong, Revisit the VEC rule in high entropy alloys (HEAs) with high-throughput CALPHAD approach and its applications for material design-A case study with Al–Co–Cr–Fe–Ni system, Acta Materialia. 192 (2020) 11–19. https://doi.org/10.1016/j.actamat.2020.03.039.

[15] S. Guo, C. Ng, J. Lu, C.T. Liu, Effect of valence electron concentration on stability of fcc or bcc phase in high entropy alloys, J. Appl. Phys. 109 (2011) 103505. https://doi.org/10.1063/1.3587228.

[16] R. Chen, G. Qin, H. Zheng, L. Wang, Y. Su, Y. Chiu, H. Ding, J. Guo, H. Fu, Composition design of high entropy alloys using the valence electron concentration to balance strength and ductility, Acta Materialia. 144 (2018) 129–137. https://doi.org/10.1016/j.actamat.2017.10.058.

[17] V. Shivam, V. Sanjana, N.K. Mukhopadhyay, Phase Evolution and Thermal Stability of Mechanically Alloyed AlCrFeCoNiZn High-Entropy Alloy, Trans. Indian Inst. Met. 73 (2020) 821–

830. https://doi.org/10.1007/s12666-020-01892-1.
[18] V. Shivam, J. Basu, Y. Shadangi, M.K. Singh, N.K. Mukhopadhyay, Mechano-chemical synthesis, thermal stability and phase evolution in AlCoCrFeNiMn high entropy alloy, J. Alloys Compd. (2018). https://doi.org/10.1016/j.jallcom.2018.05.057.
[19] V. Shivam, S. Kar, G.K. Bansal, A.K. Chandan, B.K. Sahoo, G.K. Mandal, N.K. Mukhopadhyay, V.C. Srivastava, A novel Fe-rich non-equiatomic medium-entropy alloy with superior mechanical properties, J. Alloys Compd. 952 (2023) 170029. https://doi.org/10.1016/j.jallcom.2023.170029.

[20] V. Shivam, J. Basu, R. Manna, N.K. Mukhopadhyay, Local Composition Migration Induced Microstructural Evolution and Mechanical Properties Medium-Entropy Alloy, Metall. Mater. Trans. A. 52 (2021) 1777–1789. https://doi.org/10.1007/s11661-021-06188-7.

[21] H.-P. Chou, Y.-S. Chang, S.-K. Chen, J.-W. Yeh, Microstructure, thermophysical and electrical properties in AlxCoCrFeNi (0≤x≤2) high-entropy alloys, Materials Science and Engineering: B. 163 (2009) 184–189. https://doi.org/10.1016/j.mseb.2009.05.024.
[22] W.-R. Wang, W.-L. Wang, S.-C. Wang, Y.-C. Tsai, C.-H. Lai, J.-W. Yeh, Effects of Al addition on the microstructure and mechanical property of AlxCoCrFeNi high-entropy alloys, Intermetallics. 26 (2012) 44–51. https://doi.org/10.1016/j.intermet.2012.03.005.
[23] T. Roy, V. Shivam, K. Chattopadhyay, R. Manna, N.K. Mukhopadhyay, Microstructural Evolution and Mechanical Properties of Nano- Yttria Dispersed 316 L Austenitic Stainless Steel by Mechanical Alloying and Sintering, Transactions of the Indian Institute of Metals. 74 (2021) 2093–2104. https://doi.org/10.1007/s12666-021-02317-3. Authors' list incomplete
[24] S. Koul, V. Shivam, K. Chattopadhyay, R. Manna, K. Biswas, N.K. Mukhopadhyay, Development of Oxide Dispersed Austenitic Stainless Steel through Mechanical Alloying and Spark Plasma Sintering, J. Mater. Eng. Perform. 31 (2022) 9522–9533. https://doi.org/10.1007/s11665-022-06947-6.
[25] Y. Shadangi, S. Sharma, V. Shivam, J. Basu, K. Chattopadhyay, B. Majumdar, N.K. Mukhopadhyay, Fabrication of Al-Cu-Fe quasicrystal reinforced 6082 aluminium matrix nanocomposites through mechanical milling and spark plasma sintering, Journal of Alloys and Compounds. 828 (2020) 154258. https://doi.org/10.1016/j.jallcom.2020.154258.
[26] C. Suryanarayana, Mechanical Alloying: A Novel Technique to Synthesize Advanced Materials, Research. 2019 (2019) 1–17. https://doi.org/10.34133/2019/4219812.
[27] M. Vaidya, G.M. Muralikrishna, B.S. Murty, High-entropy alloys by mechanical alloying : A review, Journal of Materials Research. 34 (2019) 664–686. https://doi.org/10.1557/jmr.2019.37.
[28] N. Singh, Y. Shadangi, V. Shivam, N.K. Mukhopadhyay, MgAlSiCrFeNi low-density high entropy alloy processed by mechanical alloying and spark plasma sintering: Effect on phase evolution and thermal stability, J. Alloys Compd. 875 (2021) 159923. https://doi.org/10.1016/j.jallcom.2021.159923.
[29] H. Jain, Y. Shadangi, V. Shivam, D. Chakravarty, Dibyendu Mukhopadhya, N.K Kumar, Phaseevolution and mechanical properties of non-equiatomic Fe e Mn e Ni e Cr e Al e Si e C high entropy steel, J. Alloys Compd. 834 (2020) 155013. https://doi.org/10.1016/j.jallcom.2020.155013
[30] V. Shivam, Y. Shadangi, J. Basu, N.K. Mukhopadhyay, Alloying behavior and thermal stability of mechanically alloyed nano AlCoCrFeNiTi high-entropy alloy, J. Mater. Res. 35 (2019) 787–795. https://doi.org/10.1557/jmr.2019.5
[31] A. Munitz, S. Salhov, S. Hayun, N. Frage, Heat treatment impacts the micro-structure and mechanical properties of AlCrFeCoNi high entropy alloy, Journal of Alloys and Compounds. 683 (2016) 221–230. https://doi.org/10.1016/j.jallcom.2016.05.034.

[32] V. Shivam, J. Basu, V.K. Pandey, Y. Shadangi, N.K. Mukhopadhyay, Alloying behaviour, thermal stability and phase evolution in quinary AlCrFeCoNi high entropy alloy, Advanced Powder Technology. 29 (2018) 2221–2230. https://doi.org/10.1016/j.apt.2018.06.006.
[33] S. Mohanty, T.N. Maity, S. Mukhopadhyay, S. Sarkar, N.P. Gurao, S. Bhowmick, K. Biswas, Powder metallurgical processing of equiatomic AlCrFeCoNi high entropy alloy: Microstructure and mechanical properties, Materials Science and Engineering: A. 679 (2017) 299–313. https://doi.org/10.1016/j.msea.2016.09.062.
[34] A. Manzoni, H. Daoud, R. Völkl, U. Glatzel, N. Wanderka, Phase separation in equiatomic AlCrFeCoNi high-entropy alloy, Ultramicroscopy. 132 (2013) 212–215. https://doi.org/10.1016/j.ultramic.2012.12.015.
[35] P. Singh, D.D. Johnson, J. Tiarks, E.M.H. White, A.B. Kustas, J.W. Pegues, M.R. Jones, H. Lim, F.W. DelRio, J.D. Carroll, G. Ouyang, M.J. Abere, R. Naorem, H. Huang, T.M. Riedemann, P.G. Kotula, I.E. Anderson, N. Argibay, Theory-guided design of duplex-phase multi-principal-element alloys, Acta Mater. 272 (2024) 119952. https://doi.org/10.1016/j.actamat.2024.119952
[36] B.H. Toby, R.B. Von Dreele, GSAS-II: The genesis of a modern open-source all purpose crystallography software package, Journal of Applied Crystallography. 46 (2013) 544–549. https://doi.org/10.1107/S0021889813003531.
[37] W.C. Oliver, G.M. Pharr, An improved technique for determining hardness and elastic modulus using load and displacement sensing indentation experiments, Journal of Materials Research, 7, (1992) 1564-1583. https://doi.org/10.1557/JMR.1992.1564
[38] D. Beniwal, P.K. Ray, Learning phase selection and assemblages in High-Entropy Alloys through a stochastic ensemble-averaging model, Comput. Mater. Sci. 197 (2021) 110647. https://doi.org/10.1016/j.commatsci.2021.110647.
[39] D.D. Johnson, D.M. Nicholson, F.J. Pinski, B.L. Gyorffy, G.M. Stocks, Density-Functional Theory for Random Alloys: Total Energy within the Coherent-Potential Approximation, Phys. Rev. Lett. 56 (1986) 2088–2091. https://doi.org/10.1103/PhysRevLett.56.2088.
[40] J.P. Perdew, K. Burke, M. Ernzerhof, Generalized Gradient Approximation Made Simple, Phys. Rev. Lett. 77 (1996) 3865–3868. https://doi.org/10.1103/PhysRevLett.77.3865.
[41] P. Singh, A.V. Smirnov, D.D. Johnson, Atomic short-range order and incipient long-range order in high-entropy alloys, Phys. Rev. B. 91 (2015) 224204. https://doi.org/10.1103/PhysRevB.91.224204.
[42] P. Singh, S. Picak, A. Sharma, Y.I. Chumlyakov, R. Arroyave, I. Karaman, D.D. Johnson, Martensitic Transformation in FexMn80-xCo10Cr10 High-Entropy Alloy, Phys. Rev. Lett. 127 (2021) 115704. https://doi.org/10.1103/PhysRevLett.127.115704.
[43] P. Singh, S. Gupta, S. Thimmaiah, B. Thoeny, P.K. Ray, A.V. Smirnov, D.D. Johnson, M.J. Kramer, Vacancy-mediated complex phase selection in high entropy alloys, Acta Mater. 194 (2020) 540–546. https://doi.org/10.1016/j.actamat.2020.04.063.
[44] P. Singh, A.V. Smirnov, A. Alam, D.D. Johnson, First-principles prediction of incipient order in arbitrary high-entropy alloys: exemplified in Ti0.25CrFeNiAlx, Acta Mater. 189 (2020) 248–254. https://doi.org/10.1016/j.actamat.2020.02.063.
[45] J. Ding, Q. Yu, M. Asta, R.O. Ritchie, Tunable stacking fault energies by tailoring local chemical order in CrCoNi medium-entropy alloys, Proc. Natl. Acad. Sci. 115 (2018) 8919–8924. https://doi.org/10.1073/pnas.1808660115.
[46] P. Singh, A.V. Smirnov, D.D. Johnson, Ta-Nb-Mo-W refractory high-entropy alloys: anomalous ordering behavior and its intriguing electronic origin, Phys. Rev. Mater. 2 (2018) 055004. https://doi.org/10.1103/PhysRevMaterials.2.055004.

[47] D. Beniwal, P. Singh, S. Gupta, M.J. Kramer, D.D. Johnson, P.K. Ray, Distilling physical origins of hardness in multi-principal element alloys directly from ensemble neural network models, Npj Comput Mater. 8 (2022) 1–11. https://doi.org/10.1038/s41524-022-00842-3.
[48] D. Beniwal, P.K. Ray, FCC vs. BCC Phase Selection in High-Entropy Alloys Via Simplified and Interpretable Reduction of Machine Learning Models, Preprint at SSRN. (2022). https://doi.org/10.2139/ssrn.4106260.
[49] D. Beniwal, Jhalak, P.K. Ray, Data-Driven Phase Selection, Property Prediction and Force-Field Development in Multi-Principal Element Alloys, in: A. Verma, S. Mavinkere Rangappa, S. Ogata, S. Siengchin (Eds.), Forcefields for Atomistic-Scale Simulations: Materials and Applications, Springer Nature, Singapore, 2022: pp. 315–347. https://doi.org/10.1007/978-981-19-3092-8_16.
[50] M. Elzain, A. Gismelseed, A. Al-Rawas, A. Yousif, H. Widatallah, M. Al-Azri, M. Al-Barwani, The hyperfine properties of iron-gallium alloys, Hyperfine Interact. 237 (2016) 8. https://doi.org/10.1007/s10751-016-1221-9.
[51] J. Gou, T. Yang, X. Liu, T. Ma, Internal structure evolution of L12 variants in aged Fe-Ga alloys, Journal of Alloys and Compounds. 836 (2020) 155282. https://doi.org/10.1016/j.jallcom.2020.155282.
[52] M.R. Rahul, G. Phanikumar, Growth kinetics, microhardness and microstructure evolution of undercooled FeCoNiCuSn high entropy alloy, Materials Science and Engineering: A. 777 (2020) 139022. https://doi.org/10.1016/j.msea.2020.139022.
[53] X.J. Zuo, Y. Coutinho, S. Chatterjee, N. Moelans, Phase field simulations of FCC to BCC phase transformation in (Al)CrFeNi medium entropy alloys, Materials Theory. 6 (2022) 12. https://doi.org/10.1186/s41313-021-00034-4.